PHYSICAL REVIEW E **100**, 043108 (2019)

Transport phenomena in the Knudsen layer near an evaporating surface

Eric Bird and Zhi Liang[*]
Department of Mechanical Engineering, California State University, Fresno, California 93740, USA

(Received 21 June 2019; revised manuscript received 12 August 2019; published 16 October 2019)

Using the combination of the kinetic theory of gases (KTG), Boltzmann transport equation (BTE), and molecular dynamics (MD) simulations, we study the transport phenomena in the Knudsen layer near a planar evaporating surface. The MD simulation is first used to validate the assumption regarding the anisotropic velocity distribution of vapor molecules in the Knudsen layer. Based on this assumption, we use the KTG to formulate the temperature and density of vapor at the evaporating surface as a function of the evaporation rate and the mass accommodation coefficient (MAC), and we use these vapor properties as the boundary conditions to find the solution to the BTE for the anisotropic vapor flow in the Knudsen layer. From the study of the evaporation into a vacuum, we show the ratio of the macroscopic speed of vapor to the most probable thermal speed of vapor molecules in the flow direction will always reach the maximum value of $\sqrt{1.5}$ at the vacuum boundary. The BTE solutions predict that the maximum evaporation flux from a liquid surface at a given temperature depends on both the MAC and the distance between the evaporating surface and the vacuum boundary. From the study of the evaporation and condensation between two parallel plates, we show the BTE solutions give good predictions of transport phenomena in both the anisotropic vapor flow within the Knudsen layer and the isotropic flow out of the Knudsen layer. All the predictions from the BTE are verified by the MD simulation results.

DOI: 10.1103/PhysRevE.100.043108

I. INTRODUCTION

Evaporation is a liquid-vapor phase change process that occurs at the surface of a liquid. A fundamental understanding of the evaporation process is of great importance to a variety of industrial and environmental applications. From the standpoint of the kinetic theory [1–3], at liquid surfaces liquid molecules are emitted and change to the vapor phase, and vapor molecules strike the surface and change into the liquid phase. When the liquid is in thermal equilibrium with its saturated vapor, the microscopic evaporation rate is the same as the microscopic condensation rate, and thus no macroscopic (net) evaporation occurs. Therefore, the macroscopic evaporation process must be a nonequilibrium process.

As the net evaporation rate increases, the vapor evaporating from the liquid surface will deviate more from the equilibrium state. Hence, there is no reason to suppose that a vapor evaporating from a liquid surface is isotropic in the immediate vicinity of liquid-vapor interface [4]. Near an evaporating surface, the kinetic temperature of vapor in the direction of evaporation could be different from that perpendicular to the evaporation direction. This region is referred to as the Knudsen layer. Only when the evaporating vapor is many times of molecular mean free paths from the liquid surface, the vapor molecules will have enough time to collide with each other so that the vapor becomes isotropic. The region out of the Knudsen layer is often referred to as the region of gas-dynamic flow. One can investigate the transport phenomena in the gas-dynamics flow based on continuum transfer equations such the Fourier's law of conduction and Newton's law of viscosity [5]. To obtain the appropriate boundary conditions (BCs) for these continuum transfer equations, however, it is necessary to study the transport phenomena in the Knudsen layer [6].

Within the Knudsen layer, the continuum transfer equations turn to be invalid [4–6]. To study the transport phenomena in a nonequilibrium gas flow, one has to use the Boltzmann transport equation (BTE). To solve the BTE, one must choose an appropriate distribution function for vapor molecules in the Knudsen layer and formulate the BCs for the BTE based on the kinetic theory of gases (KTG). Although the BTE has been widely used to study the transport phenomena in the Knudsen layer in literature [5–11], the verification of the accuracy and even validity of these solutions to the BTE is very difficult. The experimental quantification of transport processes in the Knudsen layer requires a local measurement of fluid temperature and density at a very thin layer near the evaporating surfaces with sufficient accuracy, which remains challenging [12]. It is even more challenging to measure the temperatures perpendicular and parallel to the vapor flow direction to verify the temperature anisotropy of vapor in the Knudsen layer. Moreover, it is also difficult to directly measure the velocity distribution (VD) of vapor molecules in the Knudsen layer to validate the nonequilibrium VD assumed in the theoretical analysis.

To mitigate the aforementioned experimental challenges, we resort to molecular dynamics (MD) simulations. MD simulations can determine fluid properties near the evaporating surface with high fidelity, which allows us to test the accuracy of the BCs formulated by the KTG and the solutions to the BTE. Additionally, the VD of vapor molecules in the Knudsen layer can be readily determined from MD simulations, which allows us to validate the key assumption

---

[*] zliang@csufresno.edu

regarding the nonequilibrium distribution function made in the theoretical analysis. Although the temperature anisotropy near an evaporating surface has been observed in multiple MD studies [13–16], there is a lack of fundamental and quantitative understanding of the MD simulation results on how the evaporating flow properties including flow speed, density and the extent of temperature anisotropy vary in the flow direction within the Knudsen layer. Understanding the transport phenomena in Knudsen layer requires the treatment from the BTE. To address the above-described gap in our knowledge, we use the combination of the KTG, BTE, and MD simulations to study transport phenomena in the Knudsen layer near an evaporating surface.

In this work, we consider a simple case of evaporation of a monoatomic liquid. Using the combination of the KTG, BTE and MD simulations, we study the mass, momentum and energy transfer in the Knudsen layer near an evaporating surface. In Sec. II, we introduce the key assumptions made in the theoretical analysis. Applying these assumptions to the KTG, we derive the BCs at the evaporating surface for the BTE. In Sec. III, we discuss the moment solution to the BTE and the speculations about the transport phenomena from the BTE solutions. In Sec. IV, we use MD simulations to validate the key assumptions made in the theoretical analysis. In Sec. V we carry out MD simulations to study two evaporation cases: (1) evaporation into a vacuum and (2) evaporation and condensation between two parallel plates. The MD simulation results will be used to verify the predictions from the BTE solutions. Finally, we close with conclusions.

II. THE TEMPERATURE ANISOTROPY DERIVED FROM THE KTG

A. The velocity distribution (VD) function

First, we use the KTG to study the transfer of mass, momentum and energy at an evaporating liquid surface as shown in Fig. 1. In Fig. 1, the evaporating vapor flows in the positive x direction with an average (macroscopic) velocity of v_a. The origin of the x coordinate is located at the liquid surface. It is commonly assumed that the distribution function of molecules emitted from the liquid surface at a temperature of T_L has the form [4,5]

$$f_L(v_x, v_y, v_z) = \rho_g(T_L)\left(\frac{m}{2\pi k_B T_L}\right)^{\frac{3}{2}} e^{-\frac{m(v_x^2+v_y^2+v_z^2)}{2k_B T_L}}, \tag{1}$$

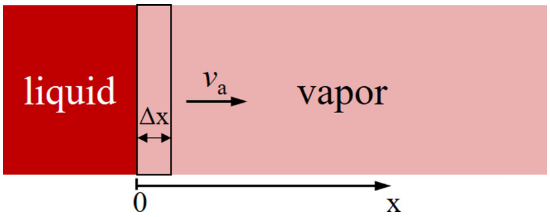

FIG. 1. The schematic diagram of the one-dimensional (1D) steady-state evaporation of a monoatomic liquid to its own vapor. v_a is the average local velocity of vapor evaporated from the liquid surface.

where $\rho_g(T_L)$ is the saturated vapor density at a temperature of T_L, m is the mass of fluid molecule, k_B is the Boltzmann constant, v_x, v_y, and v_z are velocity components in the x, y, and z directions, respectively. Accordingly, the molar, momentum and energy flux of fluid molecules emitted from the liquid surface is given by Eqs. (2a), (2b), and (2c), respectively [3,12,17]:

$$J_L^+ = \rho_g(T_L)\sqrt{\frac{k_B T_L}{2\pi m}}, \tag{2a}$$

$$M_L^+ = \rho_g(T_L)\frac{k_B T_L}{2m}, \tag{2b}$$

$$E_L^+ = \rho_g(T_L) k_B T_L \sqrt{\frac{2k_B T_L}{\pi m}}. \tag{2c}$$

To determine the net molar, momentum and energy flux at liquid surface, one also needs to know the molar, momentum and energy flux of vapor molecules that strike the liquid surface. To this end, one must choose an appropriate distribution function for vapor molecules near the evaporating surface. Multiple distribution functions were proposed in literature to describe the nonequilibrium behavior of vapor within the Knudsen layer [4–6]. To account for the anisotropy in the vapor near the evaporating surface, we use Crout's approximation [4] to assign two temperatures to the anisotropic vapor. Accordingly, the local distribution function of vapor molecules near the liquid surface is given by

$$f(v_x, v_y, v_z, x) = \rho_v(x)\sqrt{\frac{m}{2\pi k_B T_x(x)}}\, e^{-\frac{m(v_x - v_a(x))^2}{2k_B T_x(x)}} \left(\frac{m}{2\pi k_B T_y(x)}\right) e^{-\frac{m(v_y^2+v_z^2)}{2k_B T_y(x)}}, \tag{3}$$

where $\rho_v(x)$ is the local vapor density, $v_a(x)$ is the local average (macroscopic) velocity of vapor, T_x and T_y are temperatures parallel and perpendicular to the vapor flow direction, respectively. In this work, we will use MD simulations to directly determine the VD of vapor molecules near the evaporating liquid surface and validate the distribution function approximation shown in Eq. (3).

Using the distribution function in Eq. (3), one can readily obtain the molar (J_v), momentum (M_v), and energy (E_v) flux of vapor molecules moving in the positive (+) and negative (–) x directions:

$$J_v^\pm = \rho_v\sqrt{\frac{k_B T_x}{2\pi m}}\,\Gamma(\pm v_R), \tag{4a}$$

$$M_v^\pm = \rho_v\frac{k_B T_x}{m}\,\Phi(\pm v_R), \tag{4b}$$

$$E_v^\pm = \rho_v k_B T_x\sqrt{\frac{k_B T_x}{2\pi m}}\,\mathrm{E}(\pm v_R), \tag{4c}$$

where v_R, is the ratio of the macroscopic speed of vapor, v_a, to the most probable thermal speed of vapor molecules in the x direction:

$$v_R = v_a\Big/\sqrt{2k_B T_x/m}. \tag{5}$$

In Eq. (4), $\Gamma(v_R)$, $\Phi(v_R)$, and $\mathrm{E}(v_R)$ are given by [4]

$$\Gamma(v_R) = e^{-v_R^2} + v_R\sqrt{\pi}[1+\operatorname{erf}(v_R)], \tag{6a}$$

$$\Phi(v_R) = v_R e^{-v_R^2}\big/\sqrt{\pi} + \left(\tfrac{1}{2}+v_R^2\right)(1+\operatorname{erf}(v_R)), \tag{6b}$$

$$\begin{aligned}\mathrm{E}(v_R) = {}& \left(v_R^2+1+T_R\right)e^{-v_R^2} \\ &+ \sqrt{\pi}v_R\left(\tfrac{3}{2}+T_R+v_R^2\right)(1+\operatorname{erf}(v_R)),\end{aligned} \tag{6c}$$

where $T_R = T_y/T_x$. Based on the aforementioned approximations of the VD functions, we study the net mass, momentum and energy transfer at a liquid surface undergoing a steady-state evaporation in the following sections. By applying mass, momentum, and energy conservation equations, we will show the relationship between the net evaporation rate and the extent of anisotropy in vapor at the evaporating surface.

B. Mass conservation at the evaporating surface

Of those molecules that are emitted from the liquid surface a fraction, α, will change to the vapor phase. The remaining part of molecules will not enter the vapor phase. The quantity α is known as the mass accommodation coefficient (MAC) [3,12,17]. Therefore, the molar flux of molecules that are emitted from the liquid surface and change to vapor is $\alpha J_L{}^+$ where $J_L{}^+$ is given by Eq. (2a). Similarly, not all vapor molecules that strike the liquid surface will change to liquid. A fraction of vapor molecules will return to vapor phase without phase change. The fraction of incident vapor molecules that are accommodated to the liquid phase is α (i.e., MAC) [2,3,12,17]. Accordingly, the molar flux of vapor molecules that cross the liquid-vapor interface and change to liquid phase is $\alpha J^-_{v,x=0}$. Therefore, the net molar flux across the liquid surface is given by

$$J_{\mathrm{net},x=0} = \alpha\left(J_L^+ - J^-_{v,x=0}\right). \tag{7}$$

Substituting Eqs. (2a) and (4a) into Eq. (7), we obtain a relation very similar to the well-known Schrage relation [3,17]

$$J_{\mathrm{net},x=0} = \alpha\sqrt{\frac{k_B}{2\pi m}}\left(\rho_g(T_L)\sqrt{T_L} - \Gamma(-v_{R,0})\rho_{v,0}\sqrt{T_{x,0}}\right), \tag{8}$$

where $\rho_{v,0}$, $T_{x,0}$, and $v_{R,0}$ represent the density, T_x, and v_R of vapor at $x=0$ (i.e., the evaporating surface), respectively. The only difference between Eq. (8) and the original Schrage relation is that we consider the temperature anisotropy in vapor near the evaporating surface while Schrage assumed isotropic temperature in vapor.

As shown in Fig. 1, the molar flux of vapor at a plane Δx away from the evaporating surface is given by

$$J_{\mathrm{net},x=\Delta x} = J^+_{v,x=\Delta x} - J^-_{v,x=\Delta x}. \tag{9}$$

Using the mass conservation in the 1D steady-state evaporation process, we have

$$J_{\mathrm{net},x=0} = J_{\mathrm{net},x=\Delta x}. \tag{10}$$

Substituting Eqs. (7) and (9) into Eq. (10) and using Lagrange's mean value theorem, Eq. (10) becomes

$$\begin{aligned}\alpha J_L^+ - \alpha J^-_{v,x=0} = {}& \left(J^+_{v,x=0} + \left.\frac{dJ_v^+}{dx}\right|_{x=x_1}\Delta x\right) \\ &-\left(J^-_{v,x=0} + \left.\frac{dJ_v^-}{dx}\right|_{x=x_2}\Delta x\right),\end{aligned} \tag{11}$$

where x_1 and x_2 lie somewhere between 0 and Δx. Rearranging Eq. (11) and letting $\Delta x \to 0$, we obtain

$$\alpha J_L^+ = J^+_{v,x=0} - (1-\alpha)J^-_{v,x=0}. \tag{12}$$

Substituting Eqs. (2a) and (4a) into Eq. (12), we have the following relation at the evaporating surface:

$$\alpha\rho_g(T_L)\sqrt{\frac{k_BT_L}{2\pi m}} = \rho_{v,0}\sqrt{\frac{k_BT_{x,0}}{2\pi m}}\Gamma_\alpha(v_{R,0}). \tag{13}$$

In Eq. (13), $\Gamma_\alpha(v_R)$ is given by

$$\Gamma_\alpha(v_R) = \alpha e^{-v_R^2} + v_R\sqrt{\pi}[(2-\alpha)+\alpha\operatorname{erf}(v_R)]. \tag{14}$$

One can easily see that $\Gamma_\alpha(v_R)$ is reduced to $\Gamma(v_R)$ [i.e., Eq. (6a)] if $\alpha = 1$. Finally, by dividing both sides of Eq. (13) by $J_L{}^+$ [i.e., Eq. (2a)], we obtain the following dimensionless equation corresponding to the mass conservation at the evaporating surface:

$$\alpha = \rho_R\sqrt{T_{x,R}}\Gamma_\alpha(v_{R,0}), \tag{15}$$

where $\rho_R = \rho_{v,0}/\rho_g(T_L)$ and $T_{x,R} = T_{x,0}/T_L$. The above derivations are similar to those in Crout's work [4]. The difference is that Crout's analysis did not take into account the MAC, α, at the evaporating surface, while our equations consider the effect of α on mass transfer at the surface.

C. Momentum and energy conservation at the evaporating interface

In the similar manner, we obtain Eq. (16) and Eq. (17) corresponding to the conservation of momentum and energy at the evaporating liquid surface, respectively:

$$\alpha M_L^+ = M^+_{v,x=0} - (1-\alpha)M^-_{v,x=0}, \tag{16}$$

$$\alpha E_L^+ = E^+_{v,x=0} - (1-\alpha)E^-_{v,x=0}. \tag{17}$$

Substituting Eqs. (2b) and (4b) into Eq. (16) and substituting Eqs. (2c) and (4c) into Eq. (17), we have the following equations at the evaporating liquid surface:

$$\alpha\rho_g(T_L)\frac{k_BT_L}{2m} = \rho_{v,0}\frac{k_BT_{x,0}}{m}\Phi_\alpha(v_{R,0}), \tag{18}$$

$$\alpha\rho_g(T_L)k_BT_L\sqrt{\frac{2k_BT_L}{\pi m}} = \rho_{v,0}k_BT_{x,0}\sqrt{\frac{k_BT_{x,0}}{2\pi m}}\mathrm{E}_\alpha(v_{R,0}), \tag{19}$$

where

$$\begin{aligned}\Phi_\alpha(v_R) = {}& (2-\alpha)v_Re^{-v_R^2}\big/\sqrt{\pi} \\ &+\left(\tfrac{1}{2}+v_R^2\right)[\alpha+(2-\alpha)\operatorname{erf}(v_R)],\end{aligned} \tag{20}$$

$$\begin{aligned}\mathrm{E}_\alpha(v_R) = {}& \alpha\left(v_R^2+1+T_R\right)e^{-v_R^2} + \sqrt{\pi}v_R\left(\tfrac{3}{2}+T_R+v_R^2\right) \\ &\times[(2-\alpha)+\alpha\operatorname{erf}(v_R)].\end{aligned} \tag{21}$$

If $\alpha = 1$, then $\Phi_\alpha(v_R)$ and $E_\alpha(v_R)$ are reduced to $\Phi(v_R)$ [i.e., Eq. (6b)] and $E(v_R)$ [i.e., Eq. (6c)], respectively.

Finally, by dividing both sides of Eq. (18) by $M_L{}^+$ [i.e., Eq. (2b)] and both sides of Eq. (19) by $E_L{}^+$ [i.e., Eq. (2c)], we obtain the following two dimensionless equations corresponding to the momentum and energy conservation at the liquid-gas interface:

$$\alpha = 2\rho_R T_{x,R}\Phi_\alpha(v_{R,0}), \tag{22}$$

$$\alpha = \tfrac{1}{2}\rho_R T_{x,R}\sqrt{T_{x,R}}\mathrm{E}_\alpha(v_{R,0}). \tag{23}$$

D. Temperature, density, and molar flux of vapor at the evaporating surface

Recent MD simulations [13,14] show that as the fluid density drops dramatically across the a-few-nm-thick interphase layer at the evaporating surface, the VD of evaporating molecules within the interphase layer changes rapidly in the flow direction, and the isotropic temperature profile in the liquid phase is rapidly split into the longitudinal T_x and transverse T_y in the flow direction within the interphase layer. Using the combination of Eqs. (15), (22), and (23), one can obtain the dimensionless temperatures, $T_{x,R}$ and $T_{y,R}$, of vapor and the dimensionless density, ρ_R, of vapor at the position right out of the interphase layer. In this work, we define the evaporating surface at the position right out of the interphase layer. For a given α, all these three dimensionless quantities are a function of dimensionless macroscopic velocity, $v_{R,0}$, of vapor only:

$$T_{x,R} = \frac{T_{x,0}}{T_L} = \left[\frac{\Gamma_\alpha(v_{R,0})}{2\Phi_\alpha(v_{R,0})}\right]^2, \tag{24a}$$

$$T_{y,R} = \frac{T_{y,0}}{T_L} = \left[\frac{\alpha e^{-v_{R,0}^2}}{2\Gamma_\alpha(v_{R,0})} - v_{R,0}^2 - \frac{3}{2}\right]\left[\frac{\Gamma_\alpha(v_{R,0})}{2\Phi_\alpha(v_{R,0})}\right]^2 + 2, \tag{24b}$$

$$\rho_R = \frac{\rho_{v,0}}{\rho_g(T_L)} = \frac{2\alpha\Phi_\alpha(v_{R,0})}{[\Gamma_\alpha(v_{R,0})]^2}. \tag{24c}$$

Furthermore, the dimensionless molar flux, J_R, of the evaporating vapor can be also written as a function of $v_{R,0}$:

$$J_R = \frac{J_{\mathrm{net},x=0}}{J_L^+} = \frac{2\sqrt{\pi}\alpha v_{R,0}}{\Gamma_\alpha(v_{R,0})}. \tag{25}$$

In Fig. 2, we plot dimensionless density, temperature and molar flux of vapor at the evaporating surface as a function of $v_{R,0}$. In the case of $\alpha = 1$, our theoretical predictions exactly reproduce Crout's results [4] as was to be expected. Our model further extends Crout's model to include the effects of MAC on mass, momentum and energy transfer at the evaporating surface. We will verify the effects of MAC predicted by our theoretical model by comparing to MD simulation results.

According to the Schrage relationship shown in Eq. (8), the evaporation process could be driven by the temperature difference T_L–T_x across the liquid-vapor interface and/or the density difference $\rho_g(T_L)$–ρ_v. Therefore, it is reasonable to see in Figs. 2(a) and 2(b) that the vapor temperature $T_{x,R}$ and the vapor density ρ_R decrease as the evaporation rates $v_{R,0}$ and J_R increase. The lower $T_{x,R}$ at higher $v_{R,0}$ can be also understood as the result of conversion from the microscopic kinetic energy in the direction of evaporation to macroscopic kinetic energy in the vapor flow. This leads to a lower $T_{x,R}$ than $T_{y,R}$ in the evaporating vapor. As shown in Fig. 2(b), the extent of anisotropy in evaporating vapor increases with increasing evaporation rate.

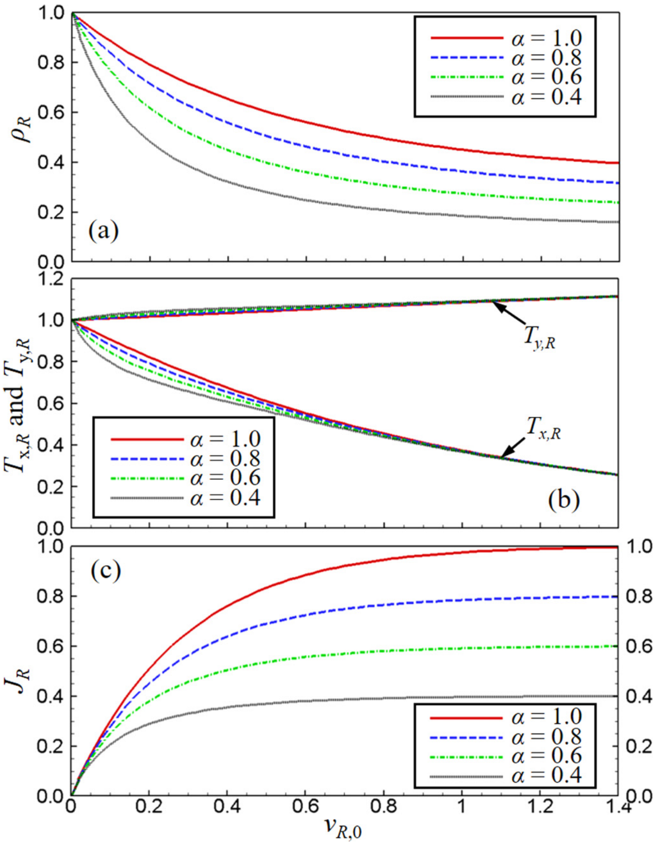

FIG. 2. The dimensionless (a) density, (b) temperature, and (c) molar flux of vapor at the evaporating surface as a function of dimensionless macroscopic velocity of vapor at the evaporating surface for different values of MAC.

With the increase of the macroscopic velocity, $v_{R,0}$, of vapor at the liquid surface, the vapor molecules that strike the liquid surface become rarer. As a result, the net evaporation flux is essentially determined by the molar flux from liquid to vapor phase, i.e., $\alpha J_L{}^+$. As shown in Fig. 2(c), the dimensionless molar flux, J_R, approaches the value of α in the limit of large $v_{R,0}$ as was to be expected. Of course, the magnitude of $v_{R,0}$ depends on the condensing BC applied at the right side of the model system.

In this section, we used the KTG to find the anisotropic temperature and density of vapor at the evaporating surface, which will be used as BCs for the BTE. In the next section, we will resort to the BTE to study the transport phenomena in the nonequilibrium vapor flow in the Knudsen layer.

III. THE BTE FOR 1D STEADY-STATE EVAPORATION

A. The BTE

We consider steady-state evaporation of a pure monoatomic fluid. For a 1D steady flow without external forces, the BTE can be written as

$$v_x \frac{\partial f}{\partial x} = Q_{\mathrm{coll}}(f), \tag{26}$$

where f is the distribution function. For an anisotropic vapor flow in the Knudsen layer near an evaporating surface, we assume the distribution function is in the form of Eq. (3). The term on the right side of Eq. (26) is the collision term accounting for the effect of collisions between molecules. To obtain the form of the collision term, $Q_{\mathrm{coll}}(f)$, we use the well-known approximation made by Bhatnagar, Gross, and Krook (BGK) [18]. The BGK approximation assumes that the molecular collisions forces a nonequilibrium distribution function, f, back to a Maxwellian equilibrium distribution function, f_e, at a rate proportional to the molecular collision frequency. Using the BGK approximation, the BTE is modified to

$$v_x \frac{\partial f}{\partial x} = \frac{(f_e - f)}{\tau}, \tag{27}$$

where τ is the molecular collision time. Since mass, momentum, and energy are conserved during molecular collisions, the local equilibrium distribution function, f_e, should have the form

$$f_e(v_x, v_y, v_z, x) = \rho_v(x)\left(\frac{m}{2\pi k_B T_e(x)}\right)^{\frac{3}{2}} e^{-\frac{m((v_x - v_a(x))^2 + v_y^2 + v_z^2)}{2k_B T_e(x)}}, \tag{28}$$

where $T_e = (T_x + 2T_y)/3$ for dilute monoatomic gases.

B. The solution to the BTE

The distribution function, Eq. (3), for the nonequilibrium vapor in the Knudsen layer contains four unknown parameters, namely, ρ_v, T_x, T_y, and v_a. To determine the variation of these four parameters in the vapor flow direction, we solve the 1D BTE by applying a four-moment method:

$$\iiint \phi v_x \frac{\partial f}{\partial x} dv_x dv_y dv_z = \iiint \phi \frac{(f_e - f)}{\tau} dv_x dv_y dv_z, \tag{29}$$

where we substitute the function ϕ with four functions, namely, 1, $\vec{v}$, $\vec{v}^2$, and v_x^2 and obtain differential Eqs. (30a) through (30d), respectively:

$$\frac{\partial}{\partial x}(\rho_v v_a) = 0, \tag{30a}$$

$$\frac{\partial}{\partial x}\left[\rho_v\left(\frac{k_B T_x}{m} + v_a^2\right)\right] = 0, \tag{30b}$$

$$\frac{\partial}{\partial x}\left[\rho_v v_a\left(\frac{1}{2}m v_a^2 + \frac{3}{2}k_B T_x + k_B T_y\right)\right] = 0, \tag{30c}$$

$$\frac{\partial}{\partial x}\left[\rho_v v_a\left(v_a^2 + \frac{3k_B T_x}{m}\right)\right] = \rho_v \frac{k_B}{m}\frac{T_e - T_x}{\tau}. \tag{30d}$$

Using Eqs. (4a)–(4c), one can readily find the net molar, momentum and energy fluxes in the vapor flow are given by

$$J_{\mathrm{net}} = \rho_v v_a, \tag{31a}$$

$$M_{\mathrm{net}} = \rho_v\left(\frac{k_B T_x}{m} + v_a^2\right), \tag{31b}$$

$$E_{\mathrm{net}} = \rho_v v_a\left(\frac{1}{2}m v_a^2 + \frac{3}{2}k_B T_x + k_B T_y\right). \tag{31c}$$

Hence, Eqs. (30a)–(30c) indicate that J_{net}, M_{net}, and E_{net} remain constant in the vapor flow direction, which is a direct result of mass, momentum and energy conservation in a steady flow. Rearranging Eqs. (30a)–(30d), we obtain the following four equations which can be used to determine the variation of ρ_v, v_a, T_x, and T_y in the vapor flow direction:

$$\frac{\partial \rho_v}{\partial x} = \frac{T_e - T_x}{\tau}\frac{\rho_v}{v_a T_x\left(2v_R^2 - 3\right)}, \tag{32a}$$

$$\frac{\partial v_a}{\partial x} = -\frac{T_e - T_x}{\tau}\frac{1}{T_x}\frac{1}{2v_R^2 - 3}, \tag{32b}$$

$$\frac{\partial T_x}{\partial x} = \frac{T_e - T_x}{\tau}\frac{1}{v_a}\frac{2v_R^2 - 1}{2v_R^2 - 3}, \tag{32c}$$

$$\frac{\partial T_y}{\partial x} = -\frac{T_e - T_x}{\tau}\frac{1}{2v_a}. \tag{32d}$$

Four BCs are required to solve the above four coupled differential equations. In Sec. II, we have derived three BCs (i.e., Eqs. (24a) through (24c)) for T_x, T_y, and ρ_v at the evaporating surface. The fourth BC will be specified at the right boundary of the model system shown in Fig. 1. Once these four BCs are known, we will solve these equations by numerical integrations.

An important parameter in the above four equations is the molecular collision frequency $1/\tau$. According to the KTG, the molecular collision frequency can be estimated by [19]

$$\frac{1}{\tau} = 4\rho_v \pi d^2 \sqrt{\frac{k_B T_e}{\pi m}}, \tag{33}$$

where d is the kinetic diameter of vapor molecules. Equation (33) shows the collision frequency, $1/\tau$, is proportional to $\rho_v\sqrt{T_e}$. Similarly, the KTG indicates the molecular mean free path, λ, is inversely proportional to the density of vapor [19]. We will see from subsequent MD simulations that the density and temperature of vapor in the Knudsen layer may change significantly in the flow direction. Therefore, it is not appropriate to assign a single value of τ or λ to the vapor molecules throughout the Knudsen layer. Moreover, the temperature anisotropy also makes it hard to define a molecular mean free path unambiguously in the nonequilibrium vapor flow. As τ and λ could vary significantly in the Knudsen layer, it is inappropriate to scale x by a constant λ, and further nondimensionalize Eqs. (32a)–(32d). Nevertheless, we are still able to speculate several general features about the transport phenomena in the Knudsen layer.

(i) Equations (32a)–(32d) all contain the term $(T_e – T_x)/\tau$. Figure 2(b) shows T_x is always lower than T_y at the evaporating surface. Hence, T_x and T_y will approach each other due to molecular collisions but will never cross each other in the Knudsen layer. As a result, $(T_e – T_x)/\tau$ should always be positive in the Knudsen layer. Therefore, Eq. (32d) indicates T_y will decrease monotonically in the flow direction. This is the result of molecular collisions in the vapor which brings T_x and T_y closer to each other.

(ii) The right side of Eqs. (32a)–(32c) contains the term $2v_R{}^2 – 3$ in the denominator. The integral of these equations will be divergent at $v_R{}^2 = 1.5$. This implies the maximum dimensionless velocity of vapor flow, v_R, should be less than $\sqrt{1.5}$. Accordingly, Eq. (32a) indicates that the vapor density, ρ_v, will decrease monotonically in the flow direction. The mass conservation requires $\rho_v v_a$ to be a constant in the flow direction. Hence, it is reasonable to see from Eq. (32b) that the vapor flow speed, v_a, will increase monotonically in the flow direction.

(iii) According to Eq. (32c), T_x will increase in the flow direction if $2v_R{}^2 – 1$ is less than zero. If $v_R{}^2$ is greater than 0.5, then T_x will decrease in the flow direction. Since Eq. (32b) shows the vapor flow velocity always increases in the flow direction and the maximum $v_R{}^2$ can approach 1.5, it is possible to observe the crossover from a negative slope to a positive slope in the T_x profile in the Knudsen layer. The variation of T_x is affected by two physical processes. First, the molecular collision process tends to increase T_x. Second, the monotonic increase of vapor flow velocity indicates a conversion from microscopic kinetic energy (i.e., thermal energy) to macroscopic kinetic energy in the vapor flow direction. The second process decreases T_x. The competition between two processes results in the variation of slope in T_x versus x profile.

All the aforementioned speculations will be verified by the MD simulations in following sections.

IV. VALIDATION OF KEY ASSUMPTIONS IN THE THEORETICAL MODEL

A. The MD model

We will use MD simulations to validate the key assumptions made in the aforementioned theoretical analyses. As depicted in Fig. 3, the typical model system consists of a liquid Ar thin film on an Au substrate. The Au substrate is formed by three (100) oriented Au atomic layers. To prevent drifting of the model system, the atoms in the leftmost Au layer are fixed in the simulation. On the right of the liquid Ar surface is its own vapor. The embedded-atom-method (EAM) potential [20] is used for Au-Au interactions. The Lennard-Jones (LJ) potential with parameters $\sigma = 3.41$ Å and $\varepsilon = 10.3$ meV [21] is employed for both Ar-Ar and Ar-Au interactions. The cutoff distance for all LJ interactions is 3.2σ. In all MD simulations we use a velocity Verlet algorithm [22] with a time step size of 4 fs to integrate the equations of motions.

The thickness of the liquid layer on the Au surface is ~6 nm which is large enough to avoid the effects of disjoining pressure on the equilibrium properties of fluid Ar [23,24]. The thickness of the liquid-vapor interfacial layer is a few nm for LJ Ar [13,14]. The left boundary of what we define as the vapor region is ~3 nm away from the liquid surface so that the vapor region does not overlap with the interfacial layer. The length of the vapor region, L_{vap}, is 100 nm as depicted in Fig. 3. To determine the variation of temperature, density and macroscopic velocity of fluid along the vapor flow direction, we evenly divide the liquid layer into six bins and divide the vapor region into ten bins in the x direction. The width of each bin in liquid and in vapor is 1 and 10 nm, respectively. The contribution from macroscopic vapor velocity is subtracted in the calculation of vapor temperature in each bin.

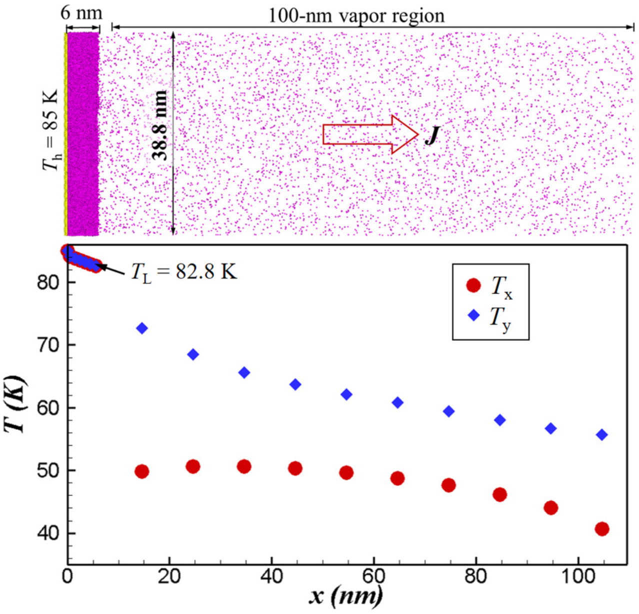

FIG. 3. (Top panel) A snapshot of the model system for the MD study of evaporation of liquid Ar on an Au surface at $T_h = 85$ K into a vacuum, and (bottom panel) the temperature profile in the vapor flow direction. The uncertainty of T_x and T_y is smaller than the size of symbols.

In the nonequilibrium MD (NEMD) simulation of the evaporation process, we maintain the temperature of the Au substrate at $T_h = 85$ K by velocity rescaling [25]. To obtain a good statistics of fluid properties, particularly in the vapor region, we set the cross-section area of the model system to 38.76 nm by 38.76 nm. Periodic boundary conditions (PBCs) are applied in the y and z directions. To further improve the accuracy of the calculated properties, ten independent runs are carried out in each case. The uncertainties of the MD simulation results are determined by analyses of these independent runs.

B. The temperature anisotropy in the Knudsen layer

An important assumption made in the aforementioned theoretical model is that the temperature of vapor is anisotropic in the Knudsen layer near an evaporating surface and the corresponding VD function of vapor is given by Eq. (3). Based on this assumption, the KTG predicts that the extent of temperature anisotropy increases with increasing evaporation rate. To exhibit an evident temperature anisotropy, therefore, we carry out a MD simulation of evaporation into a vacuum in which the maximum evaporation rates will be achieved.

To apply the vacuum BC, we remove all vapor atoms flying out the right boundary of the vapor region as shown in Fig. 3. The NEMD simulation is carried out for 3.5 ns to allow the

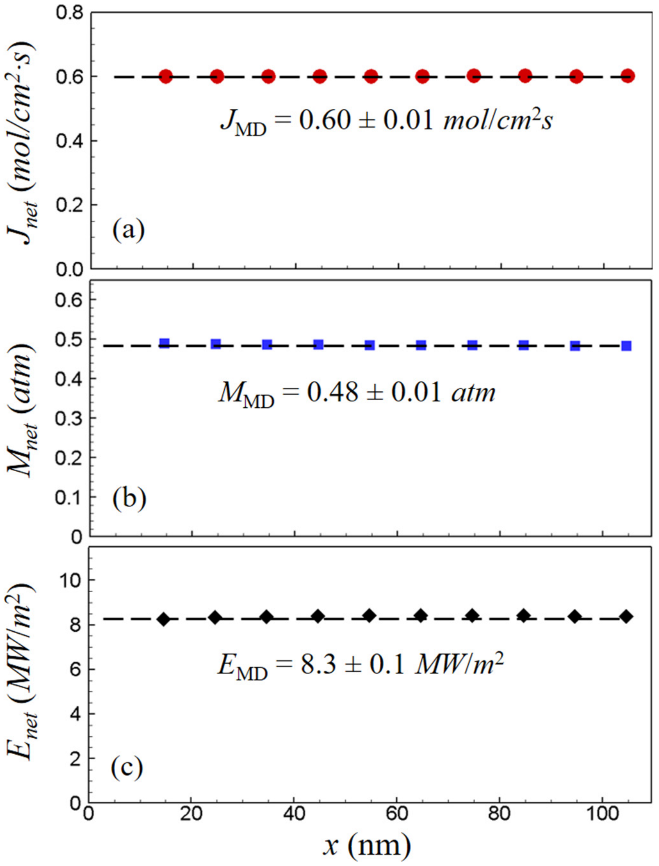

FIG. 4. The (a) molar, (b) momentum, and (c) energy flux in each bin of the vapor region. The horizontal dashed lines show the average value of molar, momentum and energy flux in the vapor region. The uncertainties are smaller than the size of symbols.

system to reach steady-state evaporation, and then additional 3.5 ns for data collection and averaging. At steady state, we calculate the density, temperature and the macroscopic vapor velocity in each bin of the simulation box. Using these vapor properties and Eqs. (31a) through (31c), we further calculate the net molar flux, J_{net}, momentum flux, M_{net}, and energy flux, E_{net}, in the vapor flow direction. It is shown in Fig. 4 that J_{net}, M_{net}, and E_{net} are constant in the vapor flow direction as was to be expected at steady state.

Now we focus on the temperature of vapor in the Knudsen layer from MD simulations. It is clearly shown in Fig. 3 that the temperature of vapor near an intensive evaporating surface is anisotropic while the temperature of liquid Ar and solid Au is isotropic. To validate the VD approximated by Eq. (3), we further calculate the VD of vapor molecules in each bin of the vapor region. In Fig. 5, we show the representative MD simulation result of VD of vapor molecules in the second bin of the vapor region where $T_x = 51$ K and $T_y = 69$ K. It is seen from Fig. 5 that the distribution of the velocity component perpendicular to the vapor flow direction closely follows the Maxwell velocity distribution (MVD) of Ar at $T = 69$ K, and the distribution of the velocity component along the flow direction agrees well with the shifted MVD (SMVD) of Ar at $T = 51$ K. The good agreement between the VD given by Eq. (3) and that obtained directly from the MD simulation is found in all other bins in the vapor region. Therefore, the VD obtained from MD simulations validates that the VD of vapor molecules near an evaporating surface can be well approximated by the distribution function given by Eq. (3).

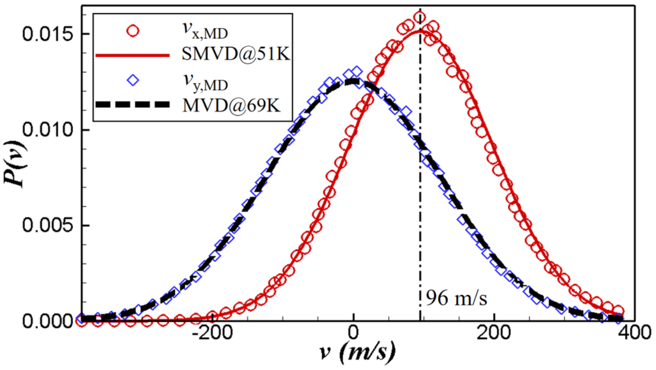

FIG. 5. The velocity distribution of vapor molecules in the second bin (∼18 nm from the evaporating surface) in the vapor region. The red circles and blue diamonds are MD simulation results for the velocity components along the vapor flow direction and perpendicular to the flow direction, respectively. The dashed line is the Maxwell velocity distribution (MVD) of Ar molecules at $T = 69$ K. The solid line is the shifted MVD (SMVD) of Ar molecules at $T = 51$ K.

To ensure the anisotropic temperature in vapor is not caused by the artifact of vacuum boundary applied in the MD simulation, we replace the vacuum boundary with a low-temperature condensing Ar surface on the right side of the simulation cell. As shown in Fig. 6, a 5-nm-thick solid Ar layer is placed on a cold Au plate maintained at $T_l = 35$ K. At such a low temperature, the saturated vapor density is

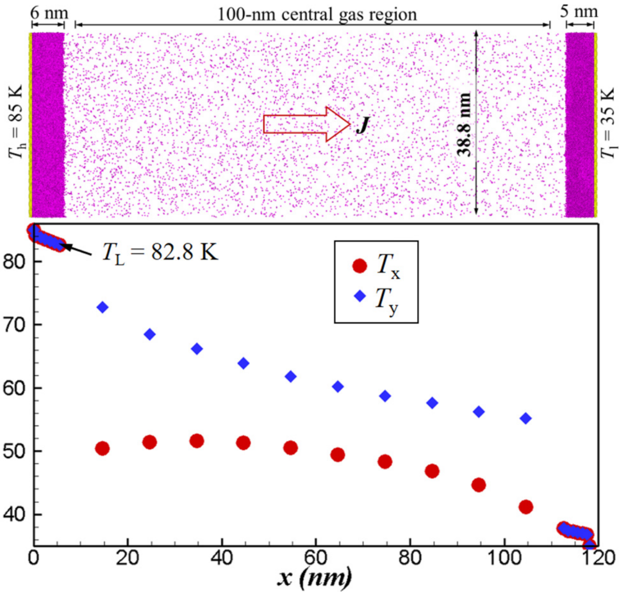

FIG. 6. (Top panel) A snapshot of the model system for the MD simulation of evaporation of liquid Ar on a hot Au surface at $T_h =$ 85 K and condensation of vapor Ar on a cold Au surface at $T_l =$ 35 K, and (bottom panel) the temperature profile in the vapor flow direction. The uncertainty of T_x and T_y is smaller than the size of symbols.

approximately zero and the MAC on the Ar surface is ~1 [23], which means all vapor Ar molecules striking on the surface will deposit on the solid Ar surface and no molecules will be emitted from the surface. Therefore, such a condensing surface should have the same effect as a vacuum boundary. In this case, the steady-state molar flux and the anisotropic temperature profile (see Fig. 6) are essentially the same as that in the case with the vacuum boundary (see Fig. 3). We further vary the temperature in the right Au plate to 0 K. The same molar flux and temperature profile in the vapor phase are obtained. Hence, the MD simulation results verify that a very cold condensing surface has the same effect as a vacuum boundary.

C. The molecular collision time

An important parameter in the BTE is the molecular collision time, τ, for the collision term in the BTE. Although the KTG gives an equation [i.e., Eq. (33)] to estimate the molecular collision time, a more accurate evaluation of τ is needed for a quantitative comparison between the MD simulation results and the solutions from the BTE. In this work, we use MD simulations to directly evaluate τ of the model fluid.

The collision time, τ, is a function of temperature and density. First, we find local temperature (T_x and T_y) and density (ρ_v) of vapor in each bin in the vapor region from the NEMD simulation described in the Sec. IV B. Second, we carry out a separate equilibrium MD (EMD) simulation in a cubic simulation box containing 500 000 Ar atoms. The box size is fixed such that the density of Ar equals to ρ_v. The PBCs are applied in all three directions. We equilibrate the vapor Ar at a temperature of T_y for 1.5 ns to let the system reach thermal equilibrium. After thermal equilibrium, we multiply the v_x of each Ar atom by $\sqrt{T_x/T_y}$ to create an initial nonequilibrium velocity distribution:

$$f_{\mathrm{ne}}(v_x, v_y, v_z, t) = \rho_v \sqrt{\frac{m}{2\pi k_B T_x(t)}} e^{-\frac{m v_x^2}{2 k_B T_x(t)}} \times \left(\frac{m}{2\pi k_B T_y(t)}\right) e^{-\frac{m(v_y^2+v_z^2)}{2 k_B T_y(t)}}. \tag{34}$$

Subsequently, we carry out an NVE simulation and monitor how T_x and T_y vary with time, t. Since the PBCs are applied in all three directions, the above distribution function is spatially independent. In this case, the BTE becomes

$$\frac{\partial f_{\mathrm{ne}}}{\partial t} = \frac{(f_{\mathrm{eq}} - f_{\mathrm{ne}})}{\tau}. \tag{35}$$

The collision between vapor molecules will bring the nonequilibrium vapor into thermal equilibrium. The equilibrium distribution function in Eq. (35) is given by

$$f_{\mathrm{eq}}(v_x, v_y, v_z) = \rho_v \left(\frac{m}{2\pi k_B T_e}\right)^{\frac{3}{2}} e^{-\frac{m(v_x^2+v_y^2+v_z^2)}{2 k_B T_e}}, \tag{36}$$

where $T_e = (T_x + 2T_y)/3$. To solve Eq. (35), we use the moment method described in Sec. III B and set $\phi = v_x^2$. Accordingly, we obtain

$$\frac{\partial T_x}{\partial t} = \frac{T_e - T_x}{\tau} \tag{37}$$

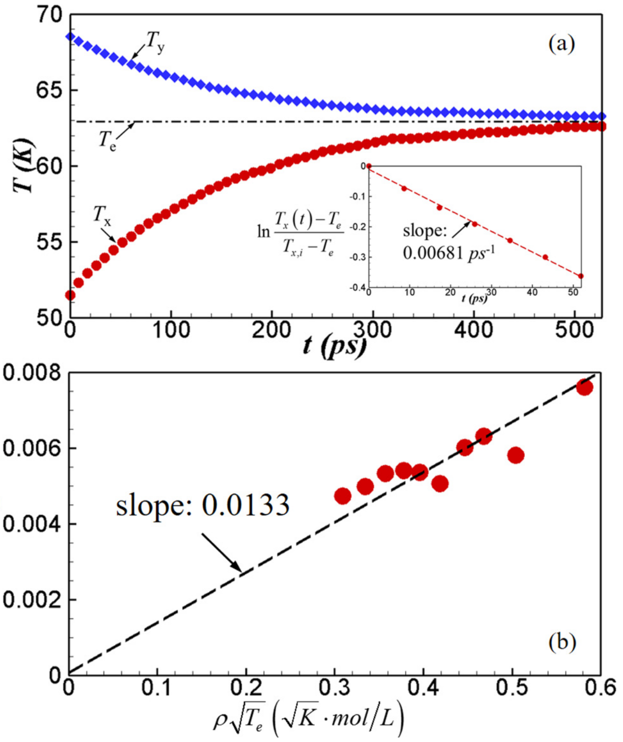

FIG. 7. (a) Dependence of T_x and T_y on t obtained from EMD simulation of vapor Ar with a density of $\rho_v = 0.0636$ mol/L and an initial temperature of $T_{x,i} = 51.5$ K and $T_{y,i} = 68.5$ K. The inset shows a linear fit of $\ln[(T_x(t)–T_e)/(T_{x,i}–T_e)]$ vs. t. (b) The dependence of molecular collision frequency, $1/\tau$, on $\rho_v\sqrt{T_e}$ obtained from MD simulations. The dashed line shows a trend line for the linear dependence between $1/\tau$ and $\rho_v\sqrt{T_e}$.

Applying the initial condition $T_x(t = 0) = T_{x,i}$, the solution to Eq. (37) is

$$\ln \frac{T_x(t) - T_e}{T_{x,i} - T_e} = -\frac{t}{\tau}. \tag{38}$$

Equation (38) indicates that we can evaluate the molecular collision time, τ, from $T_x(t)$.

In Fig. 7(a), we show the variation of T_x and T_y with t obtained from EMD simulation of vapor Ar whose density is $\rho_v = 0.0636$ mol/L and initial temperatures are $T_{x,i} = 51.5$ K and $T_{y,i} = 68.5$ K. The density and temperature are taken from the vapor property in the second bin of the vapor region in Fig. 3. The inset of Fig. 7(a) shows $\ln[(T_x(t)–T_e)/(T_{x,i}–T_e)]$ is indeed a linear function of t. This indicates the BGK approximation accurately describes the collision term for the model fluid. The slope of the linear fit gives $1/\tau = 0.00681$ ps^{-1}. Since the density and temperature of vapor are different in different bins, we use the same method to find $1/\tau$ for vapor properties in all other bins in the vapor region. The MD data in Fig. 7(b) shows $1/\tau$ is proportional to $\rho_v\sqrt{T_e}$ as was predicted by the KTG. If ρ_v and T are in units of mol/L and K, respectively, then we find from Fig. 7(b) that $1/\tau_{\mathrm{MD}} = 0.0133\rho_v\sqrt{T_e}$ ps^{-1}. For comparison, the KTG predicts the molecular collision frequency $1/\tau_{\mathrm{KTG}} = 0.0072\rho_v\sqrt{T_e}$ ps^{-1} if we use the LJ parameter $\sigma = 3.41$ Å as the kinetic diameter, d, in Eq. (33). The calculation result shows $1/\tau_{\mathrm{MD}}$ is higher than $1/\tau_{\mathrm{KTG}}$ by a factor of two. This difference can be probably explained by the following reasoning. All molecules are equivalent in the anisotropic vapor. Each collision between two molecules will bring both molecules close to equilibrium. As a result, T_x and T_y of vapor approach each other at a rate that is about two times of the molecular collision rate predicted by the KTG. We will use the τ predicted by MD simulations to solve the BTE for 1D steady-state evaporation.

V. MD VERIFICATION OF PREDICTIONS FROM THE BTE

A. The vapor property profiles in the Knudsen layer

As discussed in Sec. III B, the four-moment solution to the BTE requires four BCs. To specify the three BCs [i.e., Eqs. (24a) through (24c)] at the evaporating liquid surface, one needs to know the saturated vapor density, $\rho_g(T_L)$, and the MAC, $\alpha(T_L)$. The temperature-dependent saturated vapor density and the MAC of the model fluid Ar with a cutoff distance of 3.2σ have been determined by EMD simulations in our previous work [23]. We have successfully used the calculated $\rho_g(T_L)$ and $\alpha(T_L)$ to predict evaporation and condensation rates and thermal conductance at liquid-vapor interfaces of fluid Ar [23,26,27]. In this section, we will use the $\rho_g(T_L)$ and $\alpha(T_L)$ from our previous work in the solution to the BTE. Additionally, one also needs to know $v_{R,0}$ (i.e., v_R of vapor at the evaporating surface) to determine the three BCs, i.e., T_x, T_y, and ρ_v of vapor, at the evaporating surface. The value of $v_{R,0}$ depends on the fourth BC applied at the right boundary of the vapor region. In this section, we simply assume that $v_{R,0}$ is known, and show the general features of solutions to the BTE for different values of $v_{R,0}$. We will discuss the methods that can be used to find $v_{R,0}$ from the fourth BC in Secs. V B through 5.4.

In the following, we show the solution to the BTE for 1D steady-state evaporation of liquid Ar at a temperature of $T_L = 82.8\,\mathrm{K}$. At $T_L = 82.8\,\mathrm{K}$, our previous work [23] shows $\rho_g = 0.142\,\mathrm{mol/L}$ and $\alpha = 0.92$. We choose $T_L = 82.8\,\mathrm{K}$ because it is the temperature at the evaporating surface shown in Fig. 3. The MD simulation results will be used to verify the predictions from the BTE for different evaporation rates. In Fig. 8, we show the four-moment solution to the BTE for vapor Ar near an evaporating liquid Ar surface (located at $x = 0$) at $T_L = 82.8\,\mathrm{K}$. Each line in Fig. 8 represents the BTE prediction at a given $v_{R,0}$. According to the results shown in Fig. 2, a higher $v_{R,0}$ corresponds to a higher evaporation rate, a larger extent of temperature anisotropy and a lower density of vapor at the evaporating surface. A lower vapor density results in a lower collision rate between molecules, and thus a longer time for the anisotropic vapor to become isotropic. Hence, it is reasonable to see the thickness of the Knudsen layer (i.e., the region where T_x is different from T_y) gradually increases as the evaporation rate increases. For all cases shown in Figs. 8(c) and 8(d), ρ_v decreases monotonically and v_R increases monotonically in the vapor flow direction within the Knudsen layer as was predicted by Eqs. (32a) and (32b). In the case of $v_{R,0} = 0.6$, v_R of vapor increases to a value close to 1.224 (i.e., approximately $\sqrt{1.5}$) at $x \approx 38\,\mathrm{nm}$. At this point, the integral of Eq. (32) becomes divergent and v_R of vapor cannot increase anymore. We believe $v_R = 1.224$ at $x \approx 38\,\mathrm{nm}$ corresponds to the case of evaporation into a vacuum where the vacuum boundary is applied at the position 38 nm from the evaporating surface. To verify this speculation, we study the evaporation into a vacuum in the next section.

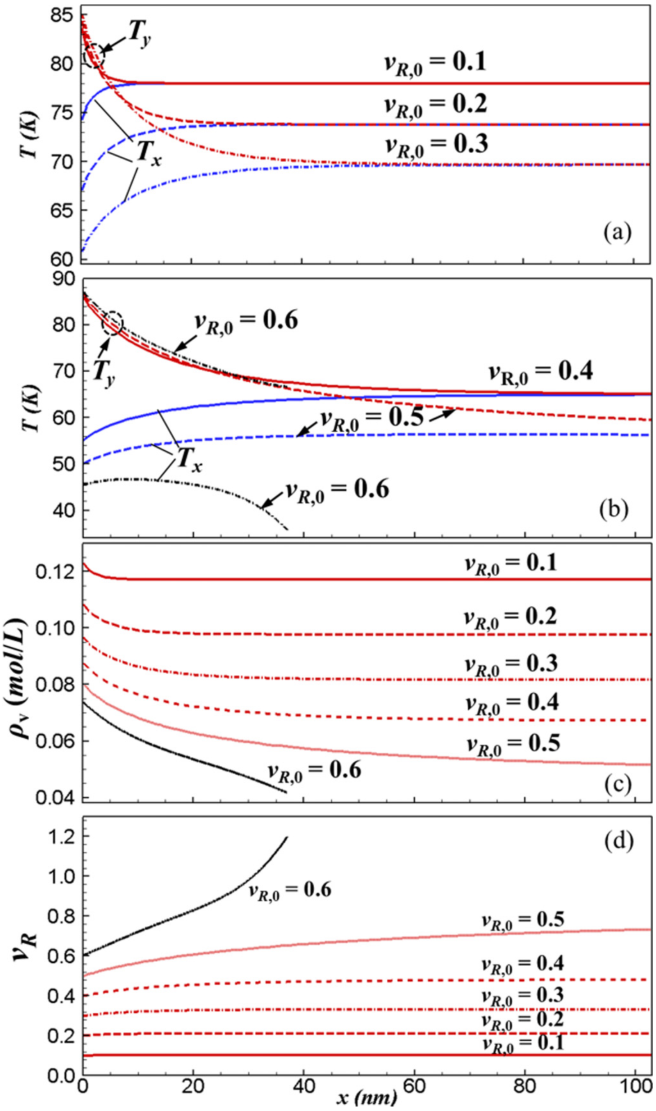

FIG. 8. The distributions of (a) and (b) temperature, (c) density, and (d) dimensionless macroscopic velocity of vapor near an evaporating liquid Ar surface (located at $x = 0$) and at a surface temperature of $T_L = 82.8\,\mathrm{K}$. The results are the prediction from the four-moment solution to the BTE. $v_{R,0}$ is the v_R of vapor at $x = 0$, i.e., the liquid-vapor interface.

B. Evaporation into a vacuum

In the case of evaporation into a vacuum, the maximum evaporation rate is achieved. When the vacuum boundary is applied, the vapor density on the right side of the vacuum boundary is zero. However, the vapor density on the left side of the vacuum boundary must not be zero. Otherwise, the macroscopic vapor velocity will be infinite according to mass conservation, which is impossible. This implies the density gradient at the vacuum boundary becomes infinite. According to Eq. (32a), the infinite density gradient is obtained when

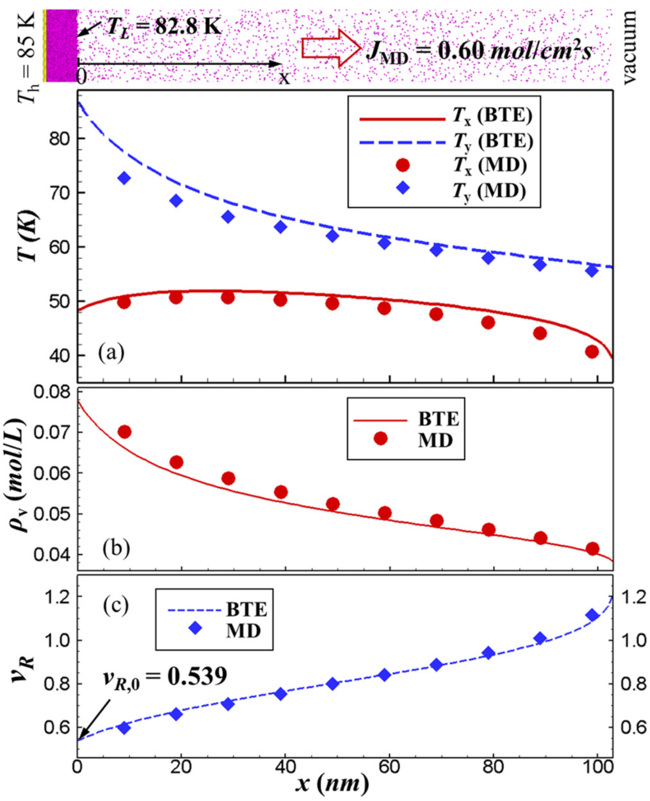

FIG. 9. (Top panel) A snapshot of the model system for the study of evaporation of liquid Ar at $T_L = 82.8$ K into a vacuum. The vacuum boundary is 103 nm from the evaporating surface. (Bottom panels) The (a) temperature, (b) density, and (c) dimensionless macroscopic velocity in the vapor region. The scatters are MD simulation results. The lines are predictions from the BTE.

$v_R = \sqrt{1.5}$. Therefore, the BC we can apply at the vacuum boundary is $v_R = \sqrt{1.5}$. Combining the BC at the vacuum boundary and the other three BCs at the evaporating surface, we have all four BCs required for the BTE.

With these four BCs, we solve the BTE for the case of evaporation of liquid Ar at $T_L = 82.8$ K into a vacuum where the vacuum boundary is located 103 nm from the liquid surface (i.e., the case shown in Fig. 3). Since three BCs are formulated at the evaporating surface and the fourth one is at the vacuum boundary, we apply a shooting method to find the solution to the BTE. In the shooting method, we gradually increase the value of $v_{R,0}$ until the integration of Eq. (32) starts to diverge at the vacuum boundary. As shown in Fig. 9(c), when $v_{R,0} = 0.539$, v_R keeps increasing in the vapor flow direction and approaches 1.224 at $x = 103$ nm. A slight increase in $v_{R,0}$ will result in a divergent integral of Eq. (32) before $x = 103$ nm. At $v_{R,0} = 0.539$, therefore, we obtain the corresponding solution to the BTE. As shown in Fig. 9, the T_x, T_y, ρ_v, and v_R profiles predicted by the BTE all agree with the MD simulation results very well. Furthermore, one can readily find from Eq. (25) that the KTG prediction of the evaporation molar flux at $v_{R,0} = 0.539$ and $T_L = 82.8$ K is 0.59 mol/cm^{2}s, which is in agreement with 0.60 ± 0.01 mol/cm^{2}s obtained directly from the MD simulation. For further reference, we estimate the mean free path of vapor molecules in the vapor region using $\lambda = 1/(\sqrt{2}\pi\rho_v d^2)$ [19]. With τ_{MD} determined from Sec. IV B and Eq. (33), we find $d \approx 0.46$ nm. Fig. 9(b) shows ρ_v reduces from 0.078 mol/L to 0.039 mol/L in the vapor region. Accordingly, the mean free path of vapor molecules increases from 22 nm at the position near the evaporating surface to 45 nm at the position close to the vacuum boundary.

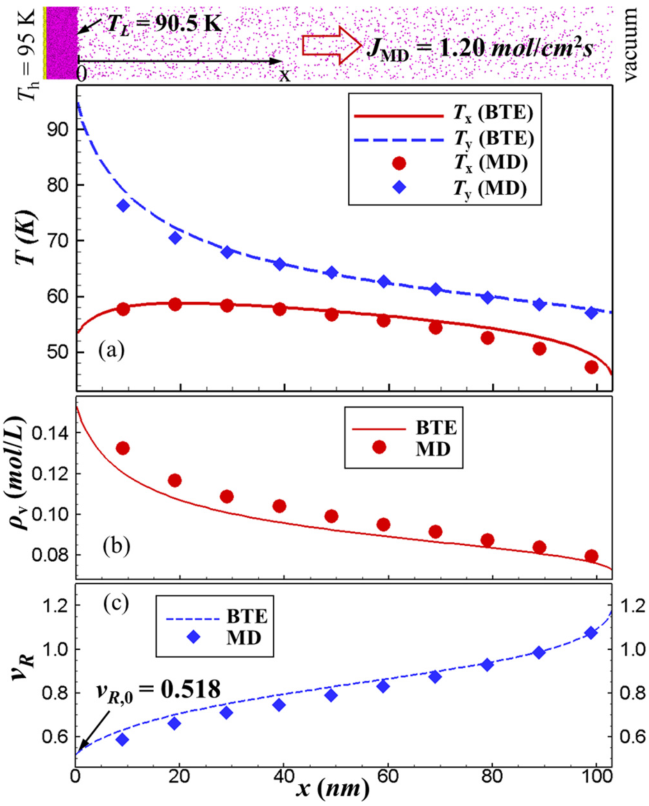

FIG. 10. Same as described in the caption of Fig. 9 except that the temperature at the evaporating surface is increased to $T_L = 90.5$ K.

As shown in Fig. 9(a), the vapor temperature is anisotropic in the vapor region, which indicates the whole vapor region is within the Knudsen layer. In the Knudsen layer, Fig. 9(a) shows T_y decreases monotonically due to the collisions between molecules in the nonequilibrium vapor. Unlike T_y, both the MD model and the BTE predict that T_x first increases in the flow direction, and then starts to decrease after it reaches the maximum value at $x \approx 30$ nm. The solution to the BTE [i.e., Eq. (32c)] predicts the maximum T_x is reached at $v_R = \sqrt{0.5}$ (i.e., ~0.707). The MD data in Fig. 9(c) show $v_R \approx 0.706$ at $x \approx 30$ nm, which verifies the crossover point of T_x profile predicted from the BTE. As we discussed in Sec. III B, the decrease of T_x in the flow direction is caused by the conversion from the thermal energy to the macroscopic kinetic energy in vapor as the vapor flow accelerates in the flow direction.

To further verify the speculations from the BTE, we increase the temperature in the Au plate to $T_h = 95$ K (see Fig. 10) and study evaporation of liquid Ar into a vacuum at a higher temperature. In this case, the temperature at the evaporating surface is $T_L = 90.5$ K, and the corresponding $\rho_g = 0.288$ mol/L and $\alpha = 0.88$ [23]. With these properties, we specify the BCs at the liquid surface and apply the aforementioned shooting method to find $v_{R,0}$ which makes v_R

TABLE I. The theoretical prediction of the dimensionless maximum evaporation flux, $J_{R,\max}$, as a function of the MAC, α, when the vacuum boundary is far from the evaporating surface. $v_{R,0}$, $T_{x,R}$, $T_{y,R}$, and ρ_R are the corresponding dimensionless macroscopic velocity, temperature, and density of vapor at an evaporating interface. The case of $\alpha = 0.92$ is highlighted because it is relevant to the MD study of evaporation of liquid Ar at $T_L = 28.2$ K into a vacuum in this work.

α	$v_{R,0}$	$J_{R,\max}$	$T_{x,R}$	$T_{y,R}$	ρ_R
1.00	0.50805	0.83843	0.60617	1.04328	0.59794
0.92	**0.50513**	**0.77994**	**0.60179**	**1.04531**	**0.56148**
0.90	0.50438	0.76514	0.60068	1.04583	0.55215
0.80	0.50059	0.69007	0.59496	1.04851	0.50415
0.70	0.49666	0.61306	0.58901	1.05132	0.45371
0.60	0.49258	0.53392	0.58281	1.05428	0.40052
0.50	0.48834	0.45245	0.57633	1.05740	0.34428
0.40	0.48391	0.36841	0.56954	1.06071	0.28458
0.30	0.47929	0.28152	0.56241	1.06422	0.22094
0.20	0.47443	0.19144	0.55490	1.06796	0.15281
0.10	0.46933	0.09776	0.54696	1.07197	0.07945

approach 1.224 at $x = 103$ nm. As shown in Fig. 10(c), we obtain the solution to the BTE when $v_{R,0} = 0.518$. At $v_{R,0} = 0.518$ and $T_L = 90.5$ K, the KTG [i.e., Eq. (25)] predicts the evaporation molar flux equals $1.17\ \mathrm{mol/cm^2 s}$, which is again in agreement with $1.20 \pm 0.01\ \mathrm{mol/cm^2 s}$ obtained directly from the MD simulation. In Fig. 10, we show the predictions from the BTE in this case also agree with the MD simulation results very well. The speculation that the maximum T_x in the vapor appears at $v_R \approx 0.707$ is again verified by the MD simulation results shown in Fig. 10.

The speculations from the BTE are also consistent with the experimental results of the evaporation of iodine to a condensing surface cooled by liquid nitrogen [9]. As we shown in Fig. 6, the condensing surface at a very low temperature is equivalent to a vacuum boundary. By means of fluorescence spectroscopy with a tunable continuous-wave dye layer, Mager et al. measured the flow velocity and the temperatures along and perpendicular to the flow direction [9]. The experimental results show v_R is approaching 1.224 at the condensing surface, which is equivalent to the vacuum boundary, and the maximum T_x is obtained at $v_R \approx 0.707$.

C. The maximum evaporation flux

The maximum evaporation flux has been extensively studied, using the KTG, in literature [3,4,10,28,29]. Most of studies assumed that the vacuum boundary is infinitely far from the evaporating surface and the MAC at the evaporating surface is 1. In this section, we will extend the existing KTG-based model to study the impact of the MAC, α, and the distance, L_{vap}, between the vacuum boundary and the evaporating surface on the maximum evaporation flux, $J_{\max}$.

To determine $J_{\max}$ from the KTG, one can define a dimensionless quantity [4]:

$$R_{\mathrm{JME}} = \frac{J_{\mathrm{net}} E_{\mathrm{net}}}{M_{\mathrm{net}}^2} \frac{2}{m}. \tag{39}$$

Substituting Eqs. (31a)–(31c) into Eq. (39), we obtain

$$R_{\mathrm{JME}} = \frac{v_R^2\left(v_R^2 + \frac{3}{2} + T_R\right)}{\left(v_R^2 + \frac{1}{2}\right)^2}, \tag{40}$$

where $T_R = T_y/T_x$. Since the net molar flux, J_{net}, momentum flux, M_{net}, and energy flux, E_{net}, remain constant in a steady flow, R_{JME} should also be constant in the vapor flow direction. If the vacuum boundary is sufficiently far from the evaporating surface, then the evaporating vapor will move through a long distance such that the vapor molecules have sufficient time to collide with each other and become isotropic before they reach the vacuum boundary. In an isotropic vapor flow, $T_R = 1$ and thus R_{JME} is a function of v_R only. Accordingly, it can be readily proved that the maximum value of R_{JME} in the isotropic vapor is 1.5625. Since R_{JME} is constant in the vapor flow direction, the maximum R_{JME} at the evaporating surface should also be 1.5625. From the theoretical analysis by Crout [4], $J_{\max}$ occurs when R_{JME} reaches the maximum value. To evaluate $J_{\max}$, we consider the expression of R_{JME} at the evaporating surface. According to Eq. (40), R_{JME} is a function of v_R and T_R. At the evaporating interface located at $x = 0$, $v_R = v_{R,0}$ and $T_R = T_{y,R}/T_{x,R}$. Equations (24a) and (24b) show both $T_{x,R}$ and $T_{y,R}$ are a function of $v_{R,0}$ and α (i.e., the MAC). Therefore, R_{JME} at the evaporating surface only depends on $v_{R,0}$ and α. For a given value of α, we can find the value of $v_{R,0}$ which makes R_{JME} reach its maximum value, i.e., 1.5625. Once the $v_{R,0}$ is known, we use Eqs. (25) and (24) to find $J_{\max}$, and the corresponding temperature and density of vapor at the evaporating interface for a given α.

In Table I, we show the dimensionless $J_{\max}$, i.e., $J_{R,\max}$, and the corresponding dimensionless vapor properties at the evaporating interface calculated from the aforementioned KTG-based model. Note that the results in Table I is obtained based on the assumption that the distance, L_{vap}, between the vacuum boundary and the evaporating surface is infinite. When $\alpha = 1$, our calculation results show $J_{\max}(L_{\mathrm{vap}} \to \infty) = 0.83843\, J_L{}^+$, where $J_L{}^+$ is given by Eq. (2a). This implies ~83.8% of the vapor molecules emitted from the liquid surface eventually leave the vacuum boundary, and ~16.2% of them return to the liquid surface due to molecular collisions in vapor [29]. This result is exactly the same as the $J_{\max}(L_{\mathrm{vap}} \to \infty)$ predicted by Crout [4]. The difference between our model and Crout's model is that we generalize Crout's model to include the effect of α on $J_{\max}$ as shown in Table I. To validate the theoretical

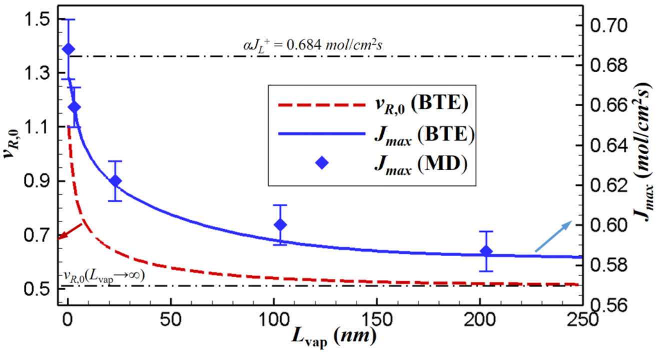

FIG. 11. The predictions from the BTE and the MD model on $v_{R,0}$ and $J_{\max}$ as a function of L_{vap} for the case of evaporation of liquid Ar at $T_L = 82.8\,\text{K}$ into a vacuum. The top horizontal dash-dot line indicates $\alpha J_L{}^+$, i.e., the molar flux of molecules that are emitted from the liquid surface and change to vapor phase. The bottom dash-dot line indicates $v_{R,0}(L_{\text{vap}} \rightarrow \infty)$, i.e., the $v_{R,0}$ predicted by the KTG shown in Table I.

predictions of $J_{\max}(L_{\text{vap}} \rightarrow \infty)$ as a function of α, we compare the calculation results to the MD simulation results.

For the model liquid Ar at $T_L = 82.8\,\text{K}$, the MD simulation shows $\rho_g = 0.142\,\text{mol/L}$ and $\alpha = 0.92$ [23]. At an evaporating surface with $\alpha = 0.92$, the KTG-based model predicts that $J_{\max}(L_{\text{vap}} \rightarrow \infty) = 0.77994\,J_L{}^+$ is achieved when $v_{R,0}(L_{\text{vap}} \rightarrow \infty) = 0.50513$ (see Table I). Using Eq. (2a), we find $J_L{}^+ = 0.744\,\text{mol/cm}^2\text{s}$ for the model liquid Ar surface at $T_L = 82.8\,\text{K}$. Accordingly, the KTG-based model predicts $J_{\max}(L_{\text{vap}} \rightarrow \infty) = 0.58\,\text{mol/cm}^2\text{s}$. To validate this prediction, we compare it to the MD simulation result. As shown in Fig. 9, $L_{\text{vap}} = 103\,\text{nm}$ in the MD model. It is clearly shown in Fig. 9(a) that 103 nm is too short to allow evaporating vapor to become isotropic. Therefore, $L_{\text{vap}} = 103\,\text{nm}$ is not long enough to be considered as $L_{\text{vap}} \rightarrow \infty$ in the model system. Although at $L_{\text{vap}} = 103\,\text{nm}$ the MD simulation shows $J_{\max,\text{MD}} = 0.60 \pm 0.01\,\text{mol/cm}^2\text{s}$ which is close to the KTG-based prediction $J_{\max}(L_{\text{vap}} \rightarrow \infty) = 0.58\,\text{mol/cm}^2\text{s}$, it is inappropriate to directly use this MD result to validate the KTG-based prediction.

To obtain $J_{\max}(L_{\text{vap}} \rightarrow \infty)$ from the MD simulation, therefore, we vary L_{vap} from 0.3 nm to 203 nm as shown in Fig. 11, determine $J_{\max}$ at each L_{vap}, and extrapolate the MD simulation results to $L_{\text{vap}} \rightarrow \infty$. To understand the dependence of $J_{\max}$ on L_{vap} found in MD simulations, we use the BTE and the shooting method described in Sec. V B to obtain $v_{R,0}$ and $J_{\max}$ at each L_{vap}. As the vacuum boundary approaches the evaporating surface, the vapor molecules emitted from the liquid surface have smaller possibility to collide with each other in the vapor region and return to liquid surface. As a result, it is seen in Fig. 11 that $v_{R,0}$ and $J_{\max}$ both increase as L_{vap} decreases. For the smallest L_{vap} (0.3 nm) in the MD study, molecules are evacuated immediately after they are emitted from the liquid surface and change to vapor. In this case, the BTE solution predicts that $v_{R,0}$ approaches 1.224 (i.e., the maximum possible v_R in the vapor) and $J_{\max} \approx 0.68\,\text{mol/cm}^2\text{s}$, which is close to $\alpha J_L{}^+ = 0.684\,\text{mol/cm}^2\text{s}$ (i.e., the molar flux of molecules that are emitted from the liquid surface and change to vapor). As L_{vap} increases, the BTE predicts that $J_{\max}$ gradually reduces to $J_{\max}(L_{\text{vap}} \rightarrow \infty) = 0.58\,\text{mol/cm}^2\text{s}$, and $v_{R,0}$ reduces to $v_{R,0}(L_{\text{vap}} \rightarrow \infty) = 0.505$. As shown in Fig. 11, the MD simulation results are consistent with the BTE predictions. In the limit of large L_{vap}, the $J_{\max}$ obtained directly from MD simulations also approaches $J_{\max}(L_{\text{vap}} \rightarrow \infty) = 0.58\,\text{mol/cm}^2\text{s}$ predicted by the KTG-based model.

The above analysis indicates that $J_{\max}$ depends on both α and L_{vap}. For an evaporating surface with a given value of α, $J_{\max}$ approaches $\alpha J_L{}^+$ if the vacuum boundary is infinitely close to the evaporating surface (i.e., $L_{\text{vap}} \rightarrow 0$). As L_{vap} increases, $J_{\max}$ decreases monotonically to $J_{\max}(L_{\text{vap}} \rightarrow \infty)$. For a given α, the dimensionless $J_{\max}(L_{\text{vap}} \rightarrow \infty)$, i.e., $J_{R,\max}$, is determined by the KTG-based model described in this section and its value can be found in Table I. The above modeling results also validate the NEMD method that was often used in literature to determine α. The NEMD method calculated the MAC, α, as the ratio of net evaporation flux into vacuum, J_{net}, to the outgoing flux, $J_L{}^+$ [14,30]. The vacuum boundary in the NEMD simulations of MAC [14] was very close to the evaporating surface. In this case, our modeling results verify that the ratio of net evaporation flux into vacuum, J_{net}, to the outgoing flux, $J_L{}^+$ equals to α.

D. Evaporation and condensation between two parallel plates

Sections V B and V C focus on the case of evaporation into a vacuum in which the whole vapor region is in the Knudsen layer. We now replace the vacuum boundary with a condensing surface and study the transport of vapor between two parallel plates. To ensure that the condensing surface is different from the vacuum boundary in the MD model,

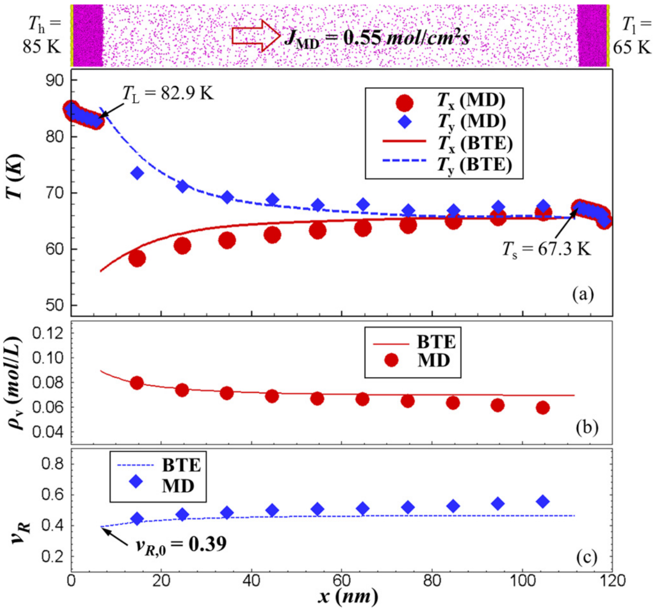

FIG. 12. (Top panel) A snapshot of the model system for the study of evaporation and condensation of fluid Ar between two parallel plates. The separation between the evaporating and the condensing surfaces is 106 nm. (Bottom panels) The (a) temperature, (b) density, and (c) dimensionless macroscopic velocity in the vapor region. The scatters are MD simulation results. The lines are predictions from the BTE.

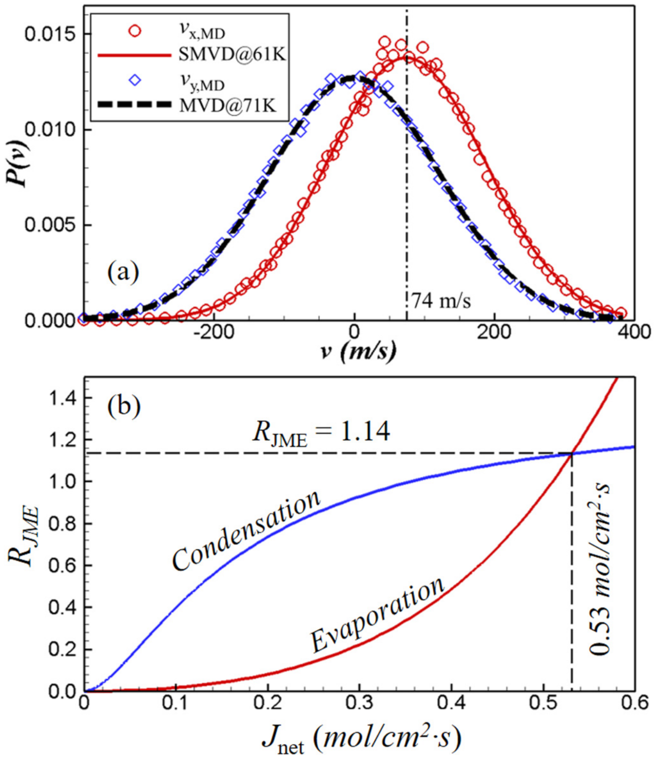

FIG. 13. (a) The velocity distribution of vapor molecules in the second bin of the vapor region. The red circles and blue diamonds are MD simulation results for the velocity components along the vapor flow direction and perpendicular to the flow direction, respectively. The dashed line is the Maxwell velocity distribution (MVD) of Ar molecules at $T = 71$ K. The solid line is the shifted MVD (SMVD) of Ar molecules at $T = 61$ K. (b) $R_{\rm JME}$ vs. $J_{\rm net}$ at the evaporating and condensing surfaces.

we increase the temperature in the right Au plate to 65 K. As shown in Fig. 12, the temperatures at the evaporating and condensing surface at steady state are 82.9 and 67.3 K, respectively. From EMD simulations of the model fluid Ar at these two temperatures [23], we obtain $\rho_g(82.9\,{\rm K}) = 0.144\,{\rm mol/L}$, $\alpha(82.9\,{\rm K}) = 0.92$ at the evaporating surface, and $\rho_g(67.3\,{\rm K}) = 0.017\,{\rm mol/L}$, $\alpha(67.3\,{\rm K}) = 1.0$ at the condensing surface. The nonzero ρ_g at the condensing surface implies the molar flux of molecules emitted from the condensing surface is nonzero. Hence, such a condensing surface is different from the vacuum boundary. The molar flux at the evaporating surface will be affected by the molecular flux emitted from the condensing surface. We will continue using the BTE and MD simulations to understand the transport phenomena of vapor in this case.

The MD simulation results shown in Figs. 12(a) and 13(a) indicate the temperature of vapor near the evaporating surface is still anisotropic in this case and the local velocity distribution of vapor molecules can be well approximated by Eq. (3). Therefore, the key assumptions made in our theoretical analysis are still valid. Since the condensing surface in this case is different from a vacuum boundary, we cannot apply the BC, $v_R = 1.224$, at the condensing surface. Instead, we can use Eqs. (24) and (25) to find the vapor temperature and molar flux at the condensing surface. The only thing we need to change in these equations is to replace $v_{R,0}$ by $v_{R,c}$, i.e., v_R at the condensing surface. The vapor flow is leaving the evaporating surface and coming to the condensing surface. Therefore, a negative $v_{R,c}$ value should be used in Eqs. (24) and (25) to find the vapor temperature and molar flux at the condensing surface.

To find the solution to the BTE, the key issue is to determine the $v_{R,0}$ at the evaporating surface. Since both $v_{R,0}$ and $v_{R,c}$ are unknown, we resort to $R_{\rm JME}$ defined in Eq. (40) to determine $v_{R,0}$. At steady state,

$$R_{{\rm JME},0} = R_{{\rm JME},c}, \tag{41}$$

where $R_{{\rm JME},0}$ and $R_{{\rm JME},c}$ are $R_{\rm JME}$ at the evaporating and condensing surfaces, respectively. Since α at the given evaporating surface is known, $R_{{\rm JME},0}$ is a function of $v_{R,0}$ only. Similarly, $R_{{\rm JME},c}$ is a function of $v_{R,c}$ only. Accordingly, there are two unknown variables, namely, $v_{R,0}$ and $v_{R,c}$ in Eq. (41). To find $v_{R,0}$, therefore, we need one more equation. Using mass conservation, we have

$$J_{{\rm net},x=0} = J_{{\rm net},c}. \tag{42}$$

According to Eq. (25), $J_{{\rm net},x=0}$, i.e., $J_{\rm net}$ at the given evaporating surface, is a function of $v_{R,0}$ only. Similarly, $J_{{\rm net},c}$, i.e., $J_{\rm net}$ at the given condensing surface, is a function of $v_{R,c}$ only. Thus, we have two equations for two unknown variables, i.e., $v_{R,0}$ and $v_{R,c}$. To solve these equations, we calculate $R_{{\rm JME},0}$ and $J_{{\rm net},x=0}$ as a function of $v_{R,0}$, and $R_{{\rm JME},c}$ and $J_{{\rm net},c}$ as a function of $v_{R,c}$. In Fig. 13(b), we plot $R_{\rm JME}$ versus $J_{\rm net}$ for evaporating and condensing surfaces. The intersection of the two curves satisfies both Eq. (41) and Eq. (42). It is seen in Fig. 13(b) that the KTG-based model predicts $J_{\rm net} = 0.53\,{\rm mol/cm^2 s}$ which is consistent with $J_{\rm net} = 0.55 \pm 0.01\,{\rm mol/cm^2 s}$ obtained directly from the MD simulation. From $J_{\rm net}$, we find the corresponding $v_{R,0}$ and use $v_{R,0}$ to evaluate T_x, T_y and ρ_v of vapor at the evaporating surface.

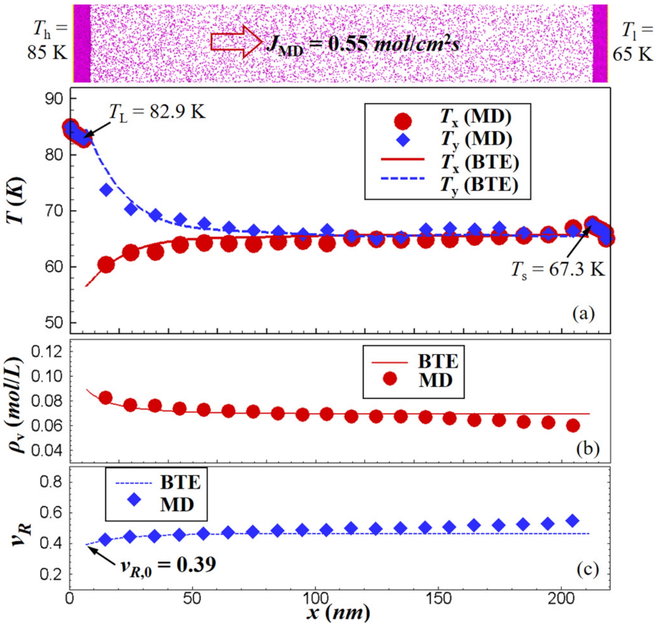

FIG. 14. Same as described in the caption of Fig. 12 except that the length of vapor region is doubled.

With these BCs, we integrate Eq. (32) to find the solution to the BTE.

It is shown in Fig. 12 that the BTE solutions are in good agreement with the MD simulation results. Eq. (32c) predicts T_x of vapor will decrease in the vapor flow direction only when υ_R is greater than 0.707. For the case studied in this section, Fig. 12(c) shows υ_R is less than 0.6 in the whole vapor region. Therefore, it is reasonable to see in Fig. 12(a) that T_x increases monotonically in the vapor flow direction. Near the right boundary of the vapor region, T_x is almost the same as T_y which means the length of the Knudsen layer in this case is comparable to that of vapor region in the model system. When we double the length of the vapor region, we clearly see a region of isotropic flow as shown in Fig. 14. In this case, the vapor region is longer than the Knudsen layer and the evaporation flux is not affected by the length of vapor region. The good agreement between the BTE predictions and the MD simulation results shown in Fig. 14 indicates that the BTE also gives a good prediction of transport phenomena of isotropic flows as was to be expected.

VI. CONCLUSIONS

In the Knudsen layer near a planar evaporating surface, the vapor temperature is anisotropic and the temperature of vapor perpendicular to the vapor flow direction (i.e., T_y) is always higher than that in the vapor flow direction (i.e., T_x). The distribution function for vapor molecules near the evaporating surface can be well approximated by Eq. (3). In the case of steady-state evaporation, the vapor density, ρ_v, and vapor temperature, T_y, decrease monotonically, and the vapor flow speed increases monotonically in the vapor flow direction in the Knudsen layer. The variation of vapor temperature, T_x, in the vapor flow direction is determined by two physical processes. One is the molecular collisions in vapor, which tends to increase T_x. The other is the energy conversion from the microscopic kinetic energy of vapor molecules to the macroscopic kinetic energy in the vapor flow direction, which tends to decrease T_x. The maximum T_x in the Knudsen layer is obtained when υ_R defined by Eq. (5) is equal to $\sqrt{0.5}$.

From the study of evaporation into a vacuum, we find the BC that can be applied at the vacuum boundary is $\upsilon_R = \sqrt{1.5}$, and $\sqrt{1.5}$ is the upper limit of υ_R in the Knudsen layer. The maximum evaporation flux from a liquid surface at a given temperature depends on both the MAC, α, and the distance, L_{vap}, between the evaporating surface and the vacuum boundary. As L_{vap} increases from 0 to ∞, the ratio of evaporation molar flux, J_{net}, to the molar flux of molecules emitted from the liquid surface, $J_L{}^+$, decreases from α to $J_{R,\max}$, where $J_{R,\max}$ is a function of α only and its value is given in Table I. From the study of the evaporation and condensation between two parallel plates, we show the BTE solutions give good predictions of transport phenomena in both the anisotropic vapor flow within the Knudsen layer and the isotropic flow out of the Knudsen layer. All the predictions from the KTG and BTE combined theoretical model are verified by MD simulations in this work.

This study focused on evaporation of monoatomic fluids. It is imperative in the future to extend the theoretical and MD model in this work to investigate evaporation of more complex fluids such as water and organic fluids.

ACKNOWLEDGMENTS

This work is supported by NSF CBET Thermal Transport Processes program under Grant No. 1911433. This work is also supported by Edison International. We thank eXtreme Science and Engineering Discovery Environment (XSEDE) for providing us supercomputer resources for MD simulations under Award No. TG-CTS130030.

---

[1] H. Hertz, Ann. Phys. **253**, 177 (1882).
[2] M. Knudsen, *Kinetic Theory of Gases*, 3rd ed. (London Methuene, London, 1950).
[3] R. W. Schrage, *A Theoretical Study of Interphase Mass Transfer* (Columbia University Press, New York, 1953).
[4] P. D. Crout, J. Math. Phys. **15**, 1 (1936).
[5] D. A. Labuntsov and A. P. Kryukov, Int. J. Heat Mass. Transfer **22**, 989 (1979).
[6] A. V. Gusarov and I. Smurov, Phys. Fluids **14**, 4242 (2002).
[7] D. Sibold and H. M. Urbassek, Phys. Fluids A **5**, 243 (1993).
[8] J. Fischer, Phys. Fluids **19**, 1305 (1976).
[9] R. Mager, G. Adomeit, and G. Wortberg, Theoretical and experimental investigation of strong evaporation of solids, in *Rarefied Gas Dynamics,* edited by E. P. Muntz, D. P. Weaver, and D. H. Campbell (AIAA, Washington, DC, 1989), pp. 460-469.
[10] T. Ytrehus and S. Østmo, Int. J. Multiph. Flow **22**, 133 (1996).
[11] Y. Sone, *Molecular Gas Dynamics* (Birkhauser, Boston, 2007).
[12] A. H. Persad and C. A. Ward, Chem. Rev. **116**, 7727 (2016).
[13] V. V. Zhakhovsky, A. P. Kryukov, V. Y. Levashov, I. N. Shishkova, and S. I. Anisimov, Proc. Natl. Acad. Sci. USA **116**, 18209 (2018).
[14] T. Ishiyama, T. Yano, and S. Fujikawa, Phys. Fluids **16**, 2899 (2004).
[15] T. Ishiyama, T. Yano, and S. Fujikawa, Phys. Rev. Lett. **95**, 084504 (2005).
[16] R. Meland, Phys. Fluids **15**, 3244 (2003).
[17] V. P. Carey, *Liquid–Vapor Phase-Change Phenomena* (Hemisphere, Publishing House, New York, 1992).
[18] P. L. Bhatnagar, E. P. Gross, and M. Krook, Phys. Rev. **94**, 511 (1953).
[19] Donald A. McQuarrie and John D. Simon, *Molecular Thermodynamics* (University Science Books, Sausalito, CA, 1999).
[20] S. M. Foiles, M. I. Baskes, and M. S. Daw, Phys. Rev. B **33**, 7983 (1986).
[21] G. C. Maitland, M. Rigby, E. B. Smith, and W. A. Wakeham, *Intermolecular Forces: Their Origin and Determination* (Clarendon Press, Oxford, 1981).
[22] D. Frenkel and B. Smit, *Understanding Molecular Simulation* (Academic Press, San Diego, 2002).
[23] Z. Liang, T. Biben, and P. Keblinski, Int. J. Heat Mass Transfer **114**, 105 (2017).

[24] J. Yu and H. Wang, Int. J. Heat Mass Transfer **55**, 1218 (2012).
[25] P. Jund and R. Jullien, Phys. Rev. B **59**, 13707 (1999).
[26] Z. Liang and P. Keblinski, J. Chem. Phys. **148**, 064708 (2018).
[27] J. Gonzalez, J. Ortega, and Z. Liang, Int. J. Heat Mass Transfer **126**, 1183 (2018).
[28] S. H. Algie, Vacuum **26**, 503 (1976).
[29] J. Safarian and T. A. Engh, Metal. Mater. Trans. A **44**, 747 (2013).
[30] M. Kon, K. Kobayashi, and M. Watanabe, Int. J. Heat Mass Transfer **99**, 317 (2016).